Surface & Coatings Technology 382 (2020) 125175

Contents lists available at ScienceDirect

Surface & Coatings Technology

journal homepage: www.elsevier.com/locate/surfcoat

Mechanical and corrosion characterization of industrially treated 316L stainless steel surfaces

L.B. Coelho[a,*], S. Kossman[b], A. Mejias[b], X. Noirfalise[c], A. Montagne[b], A. Van Gorp[b], M. Poorteman[a], M.-G. Olivier[a,c]

[a] Materials Science Department, Faculty of Engineering, University of Mons, 20 Place du Parc, 7000 Mons, Belgium
[b] Arts et Métiers, MSMP, Lille 59046, France
[c] Materia Nova asbl, Avenue Copernic 1, 7000 Mons, Belgium

ARTICLE INFO

Keywords:
Stainless steel
Electropolishing
Passivation
Corrosion
Electrochemical impedance spectroscopy
Nanoindentation

ABSTRACT

The impact of different industrial surface treatments, such as electropolishing and micro-undulation, on the mechanical and corrosion properties of cold-rolled 316L stainless steel has been investigated. The nature of the passive layers created by the three surface finishes led not only to chemical differences as determined by XPS analysis, but also to dissimilar roughness and mechanical response as shown by surface topography and nanoindentation analysis, respectively. The industrial surface treatments appeared to improve the protective anti-corrosion properties of the stainless steel as shown by electrochemical impedance analysis. Differences in re-passivation abilities were demonstrated through cyclic voltammetry and were discussed in terms of chemical profiles in the passive layer as determined from XPS. Finally, considering the passive layer as a semiconductor material, it is shown that Mott-Schottky plots are in good agreement with the chemical profile of the passive layers.

1. Introduction

The development of stainless steels dates to the end of 19th and the beginning of 20th centuries. Since then, new compositions and processing technologies have been evolving, improving their final properties. Nowadays, stainless steels are extensively produced (about 50.7 million metric tons in 2018) [1] for usage in several industries such as pharmaceutical, biomedical, automobile, aeronautical, food, building, etc. Their attractiveness is related to their high strength and principally to their outstanding corrosion resistance, which results from the presence of passive layers formed on their surface.

Although passive films are spontaneously formed upon exposure to the atmosphere, stainless steels generally pass through different surface treatments to improve their performance under service. Typical treatments can be classified into chemical, electrochemical and severe plastic deformation (SPD) processes. Among common chemical processes there are pickling, which consists in the removal of oxides to create a clean metallic surface for self-passivation, and passivation, which consists in a chemical bath that promotes the formation of the passive layers with superior properties [2,3]. Concerning the electrochemical treatments, electropolishing is one of the widely used procedures, which triggers preferential dissolution reactions in an appropriate solution upon the application of anodic currents [3,4]. SPD processes are considered as metal forming techniques, involving heavy straining under high pressure that modifies the microstructure, e.g. surface mechanical attrition (SMAT), shot peening, etc. [5,6]. In general, chemical and electrochemical treatments are principally applied to improve the corrosion resistance of stainless steel [4] and SPD processes to enhance physical, mechanical and chemical properties [5]. The chemistry of the passive films of stainless steels is definitely affected by these surface treatments, e.g., preferential dissolution of some elements during electropolishing; leading to a different mechanical response of the film and to particular corrosion resistance properties [4,7].

Apart from the corrosion resistance enhancement produced by the mentioned treatments, another important feature is the modification of surface roughness. Particularly, electropolishing is broadly used in stainless steels to reduce their roughness, giving a brilliant and shiny aspect to the surface, desired in many applications such as semiconductors and esthetic and cleaning purposes [4,8]. Roughness is a key parameter that directly affects the material performance. In the case of stainless steels the surface roughness has a strong effect on the corrosion behavior [9–11]. For instance, Hilbert et al. [10] found an improvement in the corrosion resistance of 316 stainless steel against disinfecting agents and NaCl, while reducing surface roughness by

* Corresponding author.
E-mail address: leonardo.bertoluccicoelho@umons.ac.be (L.B. Coelho).

https://doi.org/10.1016/j.surfcoat.2019.125175
Received 26 September 2019; Received in revised form 8 November 2019; Accepted 17 November 2019
Available online 19 November 2019
0257-8972/

mechanical polishing and electropolishing. Additionally, microstructural changes in stainless steels produced by surface treatments could modify their corrosion, mechanical and tribocorrosion responses [12–14]. Chen et al. [13] found a remarkable increase in the intergranular corrosion resistance of 304 stainless steel by creating a high-density twinned microstructure. Moreover, Bagherifard et al. [14] studied grain refinement produced by shot peening of 316L, which also modified the roughness, wettability and induced work hardening of the material surface.

Moreover, surface topography could affect the tribological response of these materials as well as their tribocorrosion behavior [15–17]. In this direction, this work is a first attempt to investigate the properties of 316L stainless steels (316LSS) surfaces treated by a recently developed technology (micro-undulation [18]) which produces a particular topography. Micro-undulated surfaces are claimed to present superior tribocorrosion behavior, particularly in systems susceptible to wear-corrosion solicitations. This surface treatment has shown interest to the food, agriculture and pharmaceutical industries, in applications where the transportation of suspensions presenting solutes of various types (granulates, powders, grains, flour, animal feed, etc.) are needed.

By considering the importance of surface treatments applied to stainless steels and their relevance in their resulting performance under service, this work evaluated the microstructural, chemical, mechanical and corrosion properties of 316L stainless steels with three different industrial surface finishes, namely: passivation, electropolishing-passivation and mechanochemical-electropolishing-passivation (micro-undulation).

Corrosion investigations were performed in NaCl media, since the interested industries (food, agriculture and pharmaceutical) report that chloride-based salts present either in the transported products or in the disinfecting agents eventually remain attached to the stainless steels walls, contributing for the initiation of localized corrosion processes. The achieved outcomes showed that industrial surface treatments indeed strongly modify the behavior of 316 LSS presenting the same nominal composition.

2. Materials and methods

2.1. Materials

The studied materials were 316L stainless steel plates produced by Aperam (France) undergoing different industrial surface treatments performed by Packo Inox (Belgium). The nomenclature employed to designate the three distinct treated surfaces is the following:

- SSO: passivation (followed by water rinsing). This sample was considered as the reference surface.
- SSEP: electropolishing process (bath temperature = 65 °C; current densities between 20 and 40 A/dm^2) followed by passivation.
- SSM: micro-undulation followed by electropolishing and passivation. The micro-undulation technology is a mechanochemical procedure that consists in the combination of severe plastic deformation process and acidic etching. The aim of this procedure is to produce a micro-roughness topography, which is later locally reduced in a controlled way (via electropolishing) to achieve the micro-undulated character. This technology is employed for applications in which tribocorrosion resistance is required [18].

Initially, all surfaces presented a 2B surface finish (cold rolling, annealing, pickling and light skin cold rolling; which is the most common cold rolled finishing in the industry [19,20]) prior to receiving the complementary treatments described above. It is important to emphasize that the authors do not have full access to the technical details of surface treatments due to industrial confidentiality agreements.

The composition of the specimens, as determined by X-ray fluorescence (S1 TURBOSD, Bruker, USA) in duplicate, is presented in Table 1.

Table 1
Composition (wt%) of the 316LSS samples presenting different surface treatments (0.02–0.03% C).

	Fe	Cr	Ni	Mo	Cu	Mn	Si
SSO	69.40	17.30	10.05	2.23	0.45	0.30	0.21
SSEP	69.35	17.30	10.02	2.23	0.46	0.30	0.21
SSM	69.35	17.25	10.08	2.24	0.47	0.35	0.22

No relevant chemical difference existed between SSO, SSEP and SSM.

2.2. Optical microscopy and scanning electron microscopy (SEM)

The treated surfaces were primarily observed by optical microscopy (Hirox 3D Digital Microscope, France) and then subjected to SEM analysis (Hitachi S-520, Japan). Prior to SEM observations, the surfaces were heated up at approximately 50 °C and then etched with glyceregia during 5 to 10 s (3 parts of glycerol, 3 parts of HCl and 1 part of HNO_3). Complementary SEM observations were performed after corrosion testing by employing a Hitachi SU8020 microscope (Japan).

2.3. X-ray photoelectron spectroscopy (XPS) analysis

XPS depth profile analysis was carried out on a Phi Versa Probe 5000 system (resolution 0.1 eV) using an Al Kα (1486.6 eV) radiation as the excitation source. The spectra were recorded in constant analyzer transmission mode and an estimated error of 0.1 eV was assumed for all measurements. The measurements were carried out employing an Al X-Ray source with spot size of 200 μm (50 W). The pulverization energy was equal to 500 V and thickness calibration was achieved on SiO_2/Si wafer, allowing the depth analysis to be converted from the sputtering time. Quantitative analysis was accomplished by determining the elemental peak areas, following a Shirley background subtraction. Survey spectra were recorded using 2187.85 eV pass energy with a 0.5 eV step and high-resolution XPS survey spectra were recorded using 29.5 eV pass energy with a 0.2 eV step. All spectra were corrected for the transmission function of the spectrometer.

2.4. Surface morphology characterization

The surface topography of the 316LSS plates was studied by contact and optical profilometry. Contact profilometry was performed using a Tencor (KLA-Tencor, USA). Five profiles of 8 mm length were measured in each sample with a spacing of 1 mm to calculate the roughness and waviness parameters of the samples. Optical profilometry was performed in a Veeco NT-9300 (Brucker, USA) to obtain a 3D measurement of the surface topography (~1 × 1 mm^2).

2.5. Mechanical characterization

The mechanical characterization of the stainless steel plates was performed by means of nanoindentation tests performed on the top surfaces, carried out in a Nano Indenter® XP (MTS Systems Corporation, USA) with a Berkovich diamond tip. The continuous stiffness measurement (CSM) mode was chosen for a continuous measurement of hardness and elastic modulus with penetration depth (h). The calibration of the diamond tip was performed on a fused silica sample using the CSM mode. The tests conditions were maximum penetration depth (h_{max}) 2000 nm, strain rate 0.05 s^{-1}, frequency 45 Hz and harmonic displacement 2 nm. At least 10 tests were performed for repeatability purposes.

2.6. Electrochemical characterization

All electrochemical tests were performed in 0.5 M NaCl electrolyte

by employing 316LSS coupons ultrasonically degreased in acetone (10 min). The potentiostat used was the AMETEK Parstat 2273 (Powersuite® software). The electrochemical cell comprised the stainless steels as working electrodes (~7.1 cm^2 of exposed area), an Ag/AgCl/KClsat (+197 mV/SHE) as reference electrode (RE) and a platinum coil as auxiliary electrode. All tests were conducted inside a Faraday cage and were repeated at least twice. In order to avoid substantial alteration of the treated surfaces, no cathodic step for electrochemical reduction of air-formed passive films was undertaken.

2.6.1. Polarization curves

Potentiodynamic polarization curves were obtained starting from the cathodic branch up to the anodic branch, from −600 mV to about +800 mV, at a scan rate of 0.5 mVs^{-1}. The OCP was monitored for 30 min prior to starting the test. In addition, anodic cyclic voltammetry experiments were carried out on specimens immersed for 30 min and for 58 days. In these experiments, one first forward sweep (starting from the OCP up to +650 mV) was followed by a back sweep (down to the OCP ± 50 mV) and a second forward sweep (up to +650 mV), using a scan rate of 0.5 mVs^{-1}.

Potentiostatic polarization testing was also performed by applying an anodic potential of +0.8 V for 15 min (with the aim of promoting stable pitting growth).

2.6.2. Electrochemical impedance spectroscopy

Electrochemical Impedance Spectroscopy (EIS) testing was periodically applied to the treated surfaces immersed during 57 days of immersion. A 10 mV RMS amplitude signal voltage (vs OCP) was employed, with frequencies varying between 100 kHz to 10 mHz (10 points/decade in logarithmic scale). Prior to EIS measurements, the OCP was followed for 30 min. Each individual impedance scan took about 15 min to be completed. An electrical equivalent circuit (described in the Results topic) was proposed to simulate the behavior of the passive layers present on the 316LSS surfaces.

Finally, a Mott-Schottky approach was employed to analyze the semiconducting properties of the oxide films presented on the 316LSS treated surfaces. The validity of such analysis relies on the assumption that the capacitance of the space charge layer is much smaller than that of the double layer. Hence, the capacitance determined is mainly from the contribution of the space charge layer [21]. EIS measurements were successively performed from −450 mV to +400 mV at a fixed frequency of 1 kHz [21–25] and using a potential step of 50 mV [26–28]. The scan rate of 50 mV/step was employed in order to avoid changes in the passive film [25]. One entire experiment was recorded under 15 min of immersion. The capacitance was calculated from EIS data according to Eq. (1), where ω is the angular frequency, Z″ is the imaginary part of impedance and |Z| is the impedance modulus [29]. Reproducibility of EIS results was asserted in duplicate tests.

$$C = \frac{Z''}{\omega\,|Z|^2} \quad (1)$$

3. Results and discussion

3.1. Microstructural characterization

Preliminary optical microscopy inspection was performed (Fig. 1(a)) on the stainless steel samples. The main observations were the clear cold rolling marks on the SSO surface, the well-finished surface of SSEP and the particular topography of SSM provided by the micro-undulation treatment. The cold rolling marks on SSO were no longer visible on the SSEP and SSM samples after the applied surface treatments (electropolishing and micro-undulation). With the aim of further analyzing the microstructural features of the surfaces, the samples were etched and observed by SEM (Fig. 1(b)). Working under secondary electron mode, relevant microstructural differences were revealed.

First, SSO exhibited a grain-like microstructure, as typically obtained after pickling followed by a light skin pass cold rolling stage (steps performed to obtain the surface finish 2B [10,20,30,31]. The same microstructure was observed without the SEM sample preparation protocol. Regarding the sample subjected to electropolishing process (SSEP), its surface showed a grain-like microstructure presenting twinned grains, which is characteristic of austenitic stainless steels such as the 316L. This microstructural modification was most likely related to the intrinsic removal of the material by preferential electrolytic dissolution during electropolishing [4]. This microstructure was also observed without application of the sample preparation steps, although features were easier to highlight after etching.

With respect to SSM, it presented a completely dissimilar microstructure yet: the grains showed an important degree of twinning and twin interactions (Fig. 1(b)). These microstructural changes were created by the micro-undulation process. As a result of mechanical modification processes, such as surface mechanical attrition or shot peening, intensive plastic deformation was introduced due to the particles impacting the surface under specific conditions [6,13,14,32]. In general, these processes produce grain refinement and nanostructuration of the surface [6,13,14]. Although the authors could not publish all details of the industrial micro-undulation procedure (due to confidentially agreements), we confirm that the SSM surface was subjected to an SPD process as part of the applied mechanochemical treatment.

3.2. Chemical characterization

XPS depth profile analysis was performed from the top surface of the stainless steels down to about 20 nm depth. Fig. 2 displays the achieved distributions of Fe, O, Mo, Ni, Cr (at.%) for SSO (a), SSEP (b) and SSM (c). The thickness of a passive layer might be estimated by considering that it approximately corresponds to the depth of the half-maximum O signal [33,34]. Although this definition is approximate, it suggested that thicknesses of the passive films were similar, lying somewhere between 3 and 5 nm and certainly not exceeding 10 nm (proportions of Fe were excessively high beyond this depth). Fig. 2(d), (e) and (f) shows the element ratios of Cr/Fe, Ni/Fe and Mo/Fe respectively from the external surface down to 10 nm. Relevant information could be highlighted from these fraction representations of the main alloying elements of 316L. First, the Cr/Fe ratio (d) was significantly higher for SSM and SSEP in comparison to SSO. The proportion of Cr was particularly high on the top surface of SSM. The electropolishing process (SSEP and SSM) is known for preferentially removing iron, leading to a superficial enrichment in chromium [35–37]; in agreement with the obtained results. Additionally, the Ni/Fe evolution (e) stated that the Ni proportion from the passive layer of SSO and SSEP were significantly higher than for SSM. This fact indicated that the micro-undulation process was responsible for a strong selective dissolution of Ni from the surface, probably related to the acidic etching step. Furthermore, the clearly higher proportion of Mo (f) observed for SSM might be responsible for improving the pitting resistance [38–41].

Most importantly, this elemental profile analysis pointed out to an expected enhancement of the anti-corrosion properties of SSEP and SSM, as the passivation and repassivation abilities of stainless steels are mainly related to the Cr content [42,43]. According to Luo et al. [25], a certain Cr/Fe value ratio is a necessary condition for maintaining the repassivity of stainless steels.

3.3. Surface morphology characterization

In order to assess the surface topography features of the stainless steel plates, surface profiles obtained by means of contact profilometry measurements were evaluated with the Mountains®7 software (Digital Surf, France) according to the procedure described in the ISO 4287 standard. Prior to the parameters' computation, the nominal form was

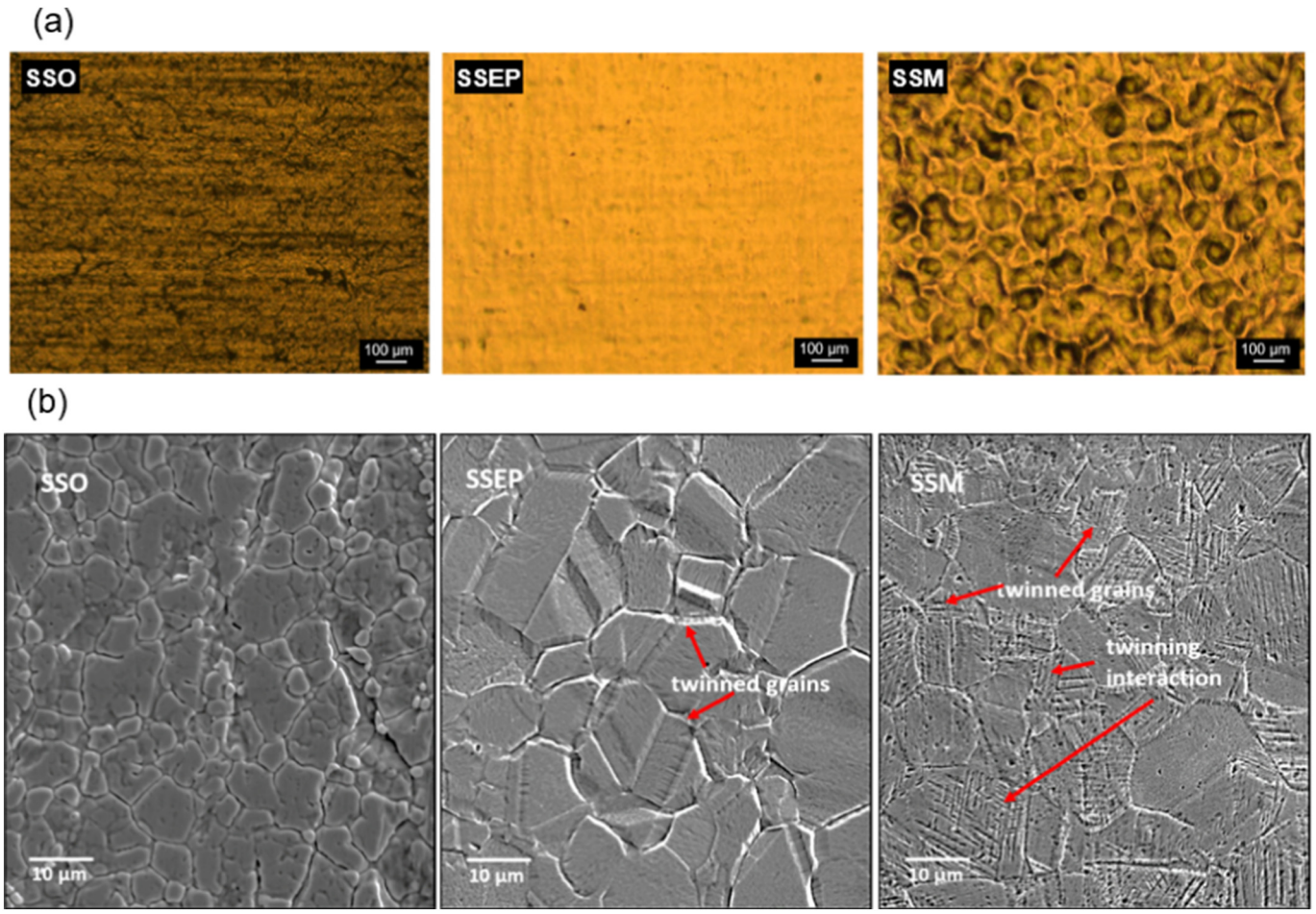

Fig. 1. (a) Optical microscopy images of the 316L stainless steel plates with the three surface treatments: SSO, SSEP and SSM. (b) SEM images in secondary electrons mode from the microstructure of 316LSS plates (SSO, SSEP, SSM). Surfaces were etched with glyceregia prior to observations according to the sample preparation protocol.

subtracted from each profile (using a 2nd degree polynomial). The achieved results are summarized in Table 2, where two typical amplitude parameters for roughness and waviness profiles respectively are presented. In Table 2 R_a is the arithmetic mean deviation of the assessed roughness profile, and R_t corresponds to the total height of the roughness profile while W_a and W_t are the equivalent parameters measured on the waviness profile [44]. Whereas the roughness is often related to surface irregularities inherent to the production process, the waviness arises from vibrations, work deflections and strains in the material.

The results displayed in Table 2 indicate that all three surfaces present R_a roughness in the nanometric scale. However, clear differences among the different surfaces can be observed. First, the electropolishing process reduced the R_a and R_t values of SSO by approximately 40% and 50%, respectively, while the waviness parameters (W_a and W_t) remained quite similar compared with SSO. Secondly, the micro-undulation process affected both roughness and waviness, leading to important modifications of the surface topography (R_a passing from ~0.10 to ~0.97 µm; W_a from 0.064 to 0.240 µm). A representative profile obtained for each sample is showed in Fig. 3, revealing the contrast between the surfaces.

Moreover, these differences between the surface topographies of the three samples were confirmed by optical profilometry (Fig. 4). These surface characterization analyses highlighted the smoothness of the SSEP surface as well as the accentuated peak-to-valley topography of SSM.

3.4. Mechanical characterization

Generally, around the indentation imprint, two deformation modes could occur: sink-in and pile-up. Sink-in arises when the material is displaced downwards underneath the indenter. Conversely, pile-up involves an upward displacement of the material during indentation. Then, according to the prevailing deformation mode, the contact area involved in the estimation of the mechanical properties varies [45]. The deformation mode depends on the E_{IT}/Y ratio (being Y the yield strength) and on the strain hardening coefficient. Typically, pile-up increases in materials with large E_{IT}/Y and little or no capacity for work hardening, because work-hardening ability inhibits pile-up formation, as the material adjacent to the indenter hardens during deformation and constrains the upward flow [46].

Sink-in was expected as the predominant deformation mode for SSO and SSEP, since 316L stainless steels typically present high strain hardening exponent and high E_{IT}/Y ratio in the annealed state [46,47]. On the contrary, the SSM surface was expected to be primarily deformed by pile-up, since plastic deformation introduced during the fabrication process is likely to diminish the strain hardening exponent as previously found by Wu et al. [47] after applying a similar surface treatment.

To confirm this first analysis, the residual imprints were investigated by optical profilometry. Then, according to the surrounding deformation (Fig. 5), sink-in was considered as the main deformation mode and the Oliver and Pharr method [46] was used for calculations concerning the SSO and SSEP samples. Conversely, for the SSM sample,

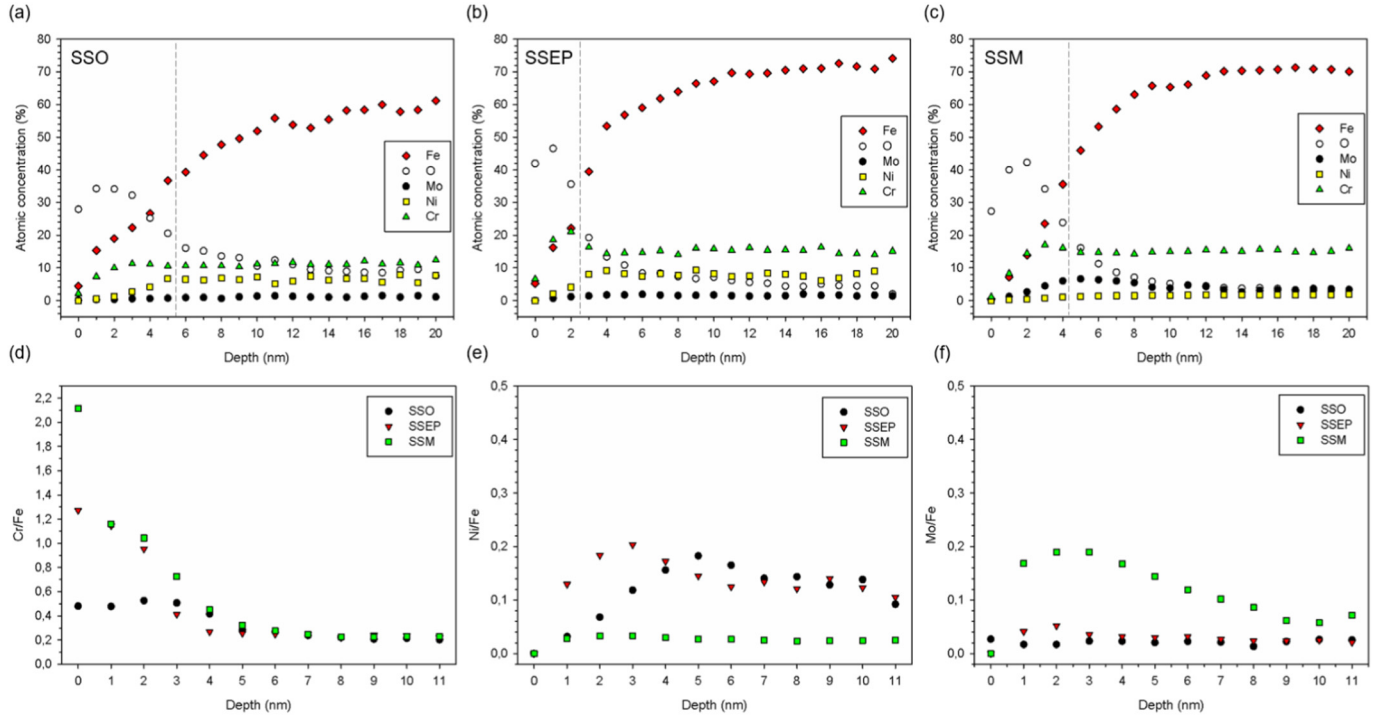

Fig. 2. XPS depth profiling of Fe, O, Mo, Ni and Cr (at.%) obtained from the top surface down to 20 nm of the 316L treated surfaces: (a) SSO; (b) SSEP; (c) SSM. Dashed lines represent the estimated positions of passive film/substrate interfaces. XPS profiling data in the form of elemental ratio of: (d) Cr/Fe, (e) Ni/Fe and (f) Mo/Fe.

Table 2
Surface morphology parameters obtained for the 316 LSS plates by contact profilometry analysis.

	R_t (μm)	R_a (μm)	W_t (μm)	W_a (μm)
SSO	2.39 ± 0.52	0.10 ± 0.01	0.56 ± 0.31	0.064 ± 0.015
SSEP	1.12 ± 0.59	0.064 ± 0.008	0.55 ± 0.19	0.073 ± 0.009
SSM	6.57 ± 0.73	0.97 ± 0.12	1.16 ± 0.19	0.240 ± 0.018

pile-up was observed and the Loubet et al. [48,49] method was then applied. The corresponding values of the hardness (H_{IT}) and the elastic modulus (E_{IT}) computed from CSM from nanoindentation tests [46] considering the previous observations are summarized in Table 3. The given values were averaged for displacements between 1500 nm and 2000 nm to avoid data affected by passive films.

The obtained elastic modulus values (Table 3) were similar, regardless the surface treatment, as anticipated because it is an intrinsic material property and should not be modified with the applied surface treatments. In contrast, hardness is modified by these treatments, the value calculated for the SSM sample was significantly higher. This increase was likely related to the extensive plastic deformation induced by the micro-undulation process [12,14], which produced microstructural changes at the surface, such as twinning (Fig. 1(b)).

Fig. 6 shows a representative example at the beginning of the load-displacement curves obtained by means of nanoindentation tests for each of the three samples. A sudden increase of penetration at constant load during the loading part of the curve, called pop-in, was observed in all SSEP curves, nonetheless, this phenomenon was absent in the two other samples (SSO and SSM). Pop-in events could be either attributed to dislocation nucleation and multiplication, to the fracture of an oxide film or material (brittle materials), or to phase transformations [50,51]. The pop-in phenomenon was registered for SSEP at an average penetration depth of 6.9 ± 1.7 nm and a corresponding average load of 13.7 ± 4.5 μN.

In the case of SSEP, pop-in events were related to the through film

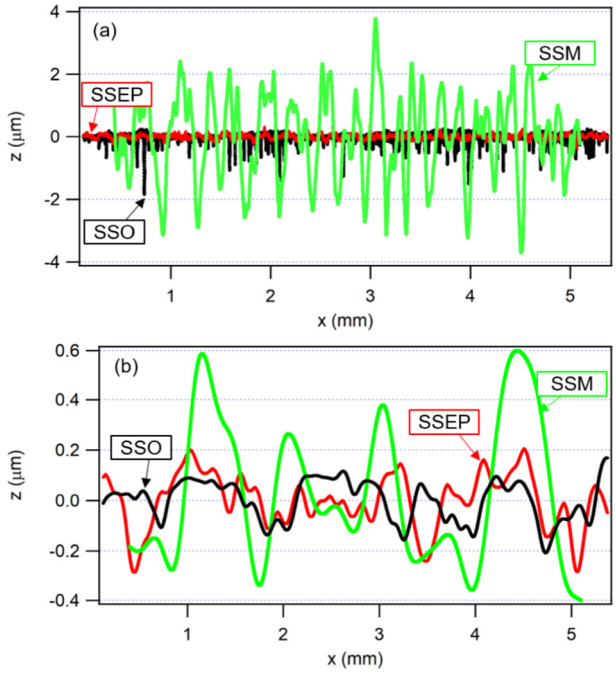

Fig. 3. Typical topography profiles of SSO, SSEP and SSM: (a) roughness and (b) waviness. The z and x axes represent the profile amplitude and length, respectively.

fracture of the passive layer, as already reported by other authors [34,51]. During indentation, elastoplastic deformation of the film/substrate system occurs. Therefore, tensile stresses are generated and promote film cracking [34,51]. The mechanical response of the film (fracture behavior and strength) is modified by the microstructure and the chemical composition; usually the film strength is related to the fracture load identified in a pop-in event on the loading curve [7,34].

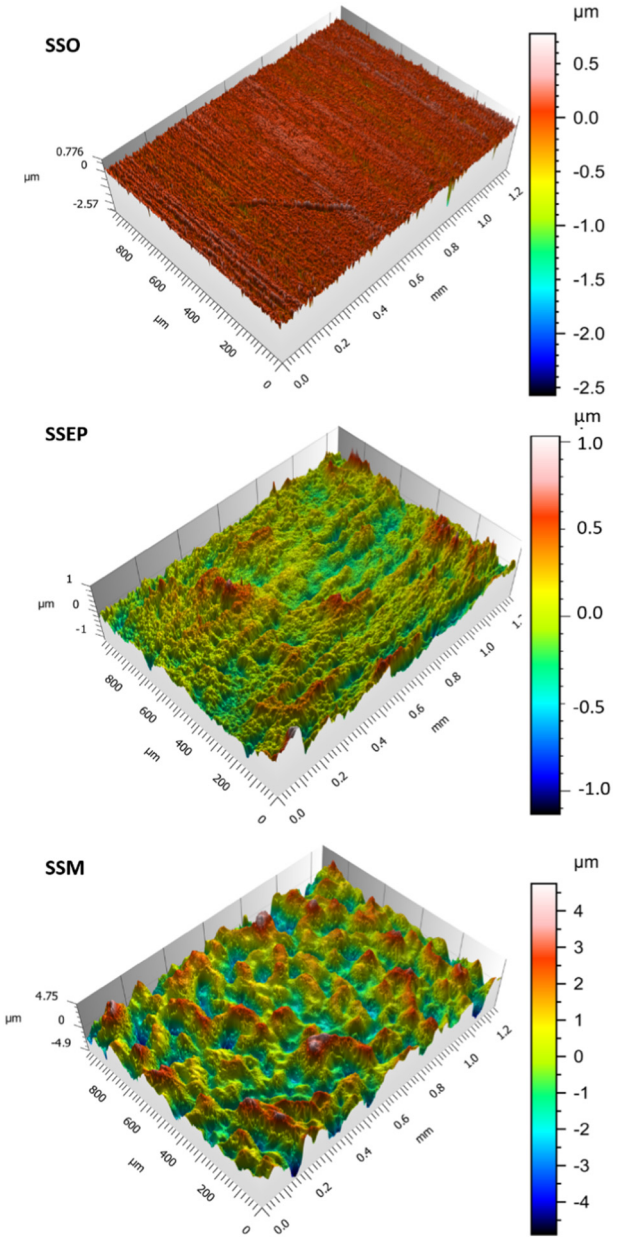

Fig. 4. Surface topography of 316L stainless steel plates obtained by optical profilometry.

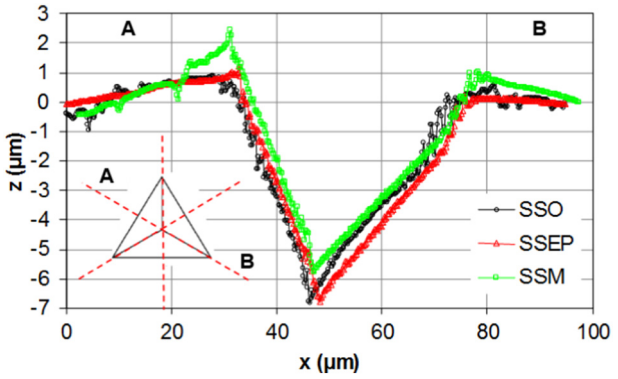

Fig. 5. Imprint profiles of the three surfaces SSO, SSEP and SSM obtained by means of optical profilometry measurements, revealing pile-up formation in the SSM sample. The tests were performed at a maximum penetration depth of 7 µm for better observation of the imprint.

Some authors agree that the strength of the passive layer increases with the increase of chromium in the top layer [34,50]. Hence, the absence of pop-in events in the load-displacement curves of the SSO and SSM samples suggests dissimilar structures and chemical compositions (e.g. crystalline, epitaxial growth [7]) of the passive film generated by the three surfaces finish processes. Accordingly, the passive films of SSO and SSM might fracture by small cracks relieving the stresses, eventually presenting imperceptible discontinuities on the load-displacement curves instead of large pop-in events as proposed by Yassar et al. [7] who found that the composition of the passive film modifies its microstructure thus altering the mechanical response.

3.5. Electrochemical characterization

3.5.1. Corrosion characterization

The corrosion behavior of the 316LSS samples was firstly assessed by means of potentiodynamic polarization method in 0.5 M NaCl electrolyte. The obtained results systematically showed that no considerable difference existed regarding the corrosion properties of the different surface treatments under potentiodynamic polarization.

For instance, Fig. 7 shows that while minor differences existed between the OCP of the different surfaces, their pitting potential E_{pit} was quite similar, being around +400 mV Vs RE. Additionally, all substrates presented quite similar passivation ranges with extensions of about 500 mV. Although in principle the electropolished and the micro-undulated surfaces were expected to present superior corrosion properties in comparison to the reference substrate, the outcomes pointed to no significant differences. With respect to the cathodic branch, it could be seen that all surfaces also presented the same behavior: a cathodic process limited by oxygen diffusion down to about −600 mV Vs RE and the activation of water reduction reaction at more negative potentials. The similar overall corrosion behavior achieved for the three surface finishes is reflective of their induced passivated state achieved industrially by a chemical passivation step.

Next, Electrochemical Impedance Spectroscopy was applied with the aim of depicting possible differences in the electrochemical response of the three types of surfaces exposed to 0.5 M NaCl.

The obtained EIS spectra were almost coincident for all substrates. Fig. 8(a) shows the EIS curves obtained immediately after potential stabilization; namely, 30 min after immersion. The impedance response comprised two indistinguishable time constants (TC) located at medium to lower frequencies and respectively related to the properties of the passive layer and of the electrical double layer. As an approximation to express the impedance properties of the passive oxide films, the superimposed relaxation processes were described by a unique time constant comprising a resistance in parallel to a capacitance (the contribution from the double layer could only be fully sensed at lower frequencies that are impracticable to be attained in practice).

The resistance of the oxide R_{ox} and the capacitance of the oxide C_{ox} could be fitted by the electrical equivalent circuit showed in Fig. 8(a). The evolution of R_{ox} and C_{ox} as a function of time up to 57 days of immersion are presented in Fig. 8(b) and Fig. 8(c), respectively. The C_{ox} was calculated from the constant phase element CPE_{ox} employed in the fitting for accounting the non-ideal behavior of the capacitor (Eq. (2)) [52]. Here, ω_{max} was considered to be 0.01 Hz, as it was the frequency at which the imaginary impedance reached a maximum for the respective TC. Fig. 8(d) displays the evolution of the n parameter, which is a mathematical artifice that allows the correlation of the fitted *CPE* to the capacitance (Eq. (2)). The *n* parameter is usually associated to the surface heterogeneity.

$$C = CPE(\omega_{max})^{n-1} \quad (2)$$

The evolution of R_{ox} (Fig. 8(b)) shows that no significant differences existed between the resistances of the three types of passive layer under investigation. Nonetheless, one might argue that the R_{ox} from SSEP, and particularly the one from SSM, were slightly higher and more stable

Table 3
Elastic modulus and hardness obtained by nanoindentation tests. Considering sink-in deformation for SSO and SSEP and pile-up deformation for SSM.

	E_{IT} (GPa)	H_{IT} (GPa)
SSO	198 ± 11	2.1 ± 0.2
SSEP	189 ± 10	2.1 ± 0.1
SSM	197 ± 9	3.6 ± 0.2

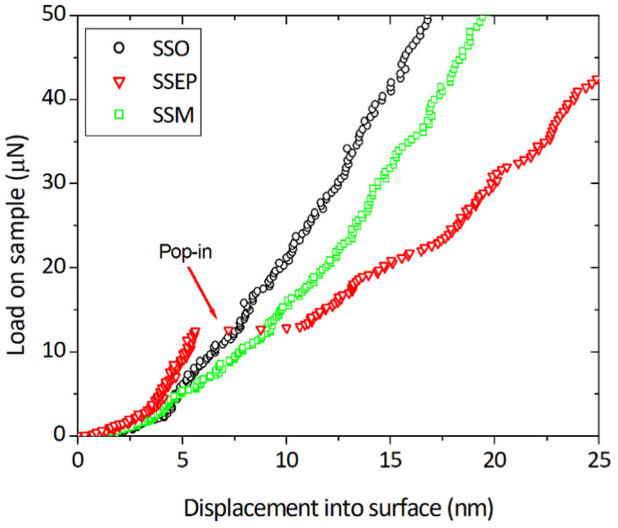

Fig. 6. Initial loading part of load-displacement curves of nanoindentation on 316L stainless steel performed on different surface treatments: SSO, SSEP, SSM. The only sample showing a pop-in event is the SSEP.

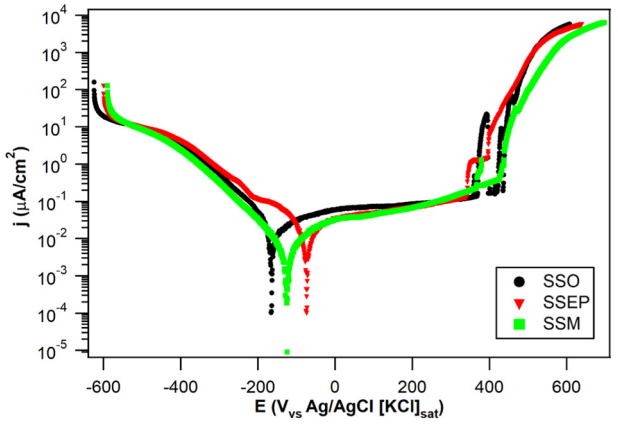

Fig. 7. Potentiodynamic polarization curves obtained in 0.01 M NaCl electrolyte for the different 316LSS surfaces (SSO, SSEP, SSM).

over time than the R_{ox} from SSO. The slight decrease in resistance depicted for SSO after 18 days suggested the relative inferior protective properties of its passive layer not subjected to electropolishing procedures.

Fig. 8(c) shows that the capacitive response was considerably higher for SSO than for SSM. As the capacitance is directly proportional to the active surface area, the SSM sample, which undoubtedly presented the roughest surface (Table 2) was expected to exhibit the highest C_{ox} values. Despite the likely greater real surface area of SSM, the higher charge accumulation detected for SSO suggested the poorer anti-corrosion properties of this substrate. Concerning the SSEP sample, regardless of its relatively smoother surface (Table 2) and consequently lower area available for electrochemical reactions, it presented a C_{ox} evolution virtually identical to the one achieved for SSM. Once again, this fact pointed out to the outstanding corrosion resistance of the passive film formed on the micro-undulated surface. The inspection of the n parameter evolution (Fig. 8(d)) reinforced the idea of the electropolished surface as the closest one to an ideal capacitor (n values around 0.95), while the passive layer of SSO seemed to be the most heterogeneous one (n values around 0.90).

Seeking at further assessing the protective properties of the dissimilar passive films formed, samples were subjected to anodic cyclic voltammetry (CV) tests in 0.5 M NaCl. Considering that no difference between the anodic branches was verified under traditional potentiodynamic polarization (Fig. 7), the CV approach here employed aimed at testing the repassivation ability of the passive layers, besides their passivation properties (E_{pit}, passivation range). Fig. 9 shows the cyclic voltammetry curves obtained for the three types of samples after 58 days of exposure to 0.5 M NaCl.

It could be seen that after 58 days, the repassivation ability of SSO was considerably worse than the other two specimens. Indeed, not only the current density (j) of SSO was the highest one achieved after passivity breakdown (group of arrows 2), but it also remained considerably higher than the current density values of SSEP and SSM during the back scan (arrows 3 and 4). Finally, during the second positive-going scan (arrows 5 and 6), the j values measured for SSO remained extremely high, indicating the poor repassivation ability of this surface. Concerning the SSEP and SSM samples, these behaved relatively similar from the first forward sweep up to the starting of the second one (arrows 1 to 5). During the final anodic sweep, although j values were relatively higher than the ones measured during the first anodic sweep, they were still significantly lower than those computed during the back scan. These results clearly demonstrated that the SSEP and SSM systems could repassivate to some extent, although passive layers formed in-operando in NaCl solution were less protective than those of the original treated surfaces. Yet, during the second forward scan (arrows 6), a vertiginous increase of j was observed for SSEP from about +0.10 V, while the anodic response of SSM remained relatively steady up to potentials as high as ~+0.44 V.

In order to better illustrate the results achieved by CV tests, Table 4 presents the following parameters extracted from the curves obtained during the first (1) and second (2) anodic sweeps: corrosion potential (E_{corr}), critical pitting potential (E_c), passivity range ($\Delta E = E_c - E_{corr}$) and current density at E = +650 mV (j_{-650}). E_c was defined as the potential in which the current presented a sharp and stable increase.

These outcomes demonstrated the enhanced anti-corrosion behavior of SSM when tested under conditions allowing repassivation phenomena. It is worth mentioning that the same CV approach was applied to the three substrates after 30 min of immersion but resulting curves were rather undistinguishable (results not presented). Therefore, although presenting virtually identical protective properties at short immersion times, such as presented in Fig. 7, the corrosion behavior of the treated surfaces tended to evolve differently upon immersion (Fig. 9), which corroborates the dissimilar evolutions of the R_{ox} curves observed as a function of time (Fig. 8(b)).

Moreover, relevant differences in the morphology of pitting were depicted for the 316 LSS samples subjected to anodic potentiostatic polarization at +0.8 V (15 min) in 0.5 M NaCl. The SEM micrographs presented in Fig. 10 show that pitting on the SSO surface comprised a high amount of relatively small pits (diameter below 100 μm). Alternatively, the pitting process on SSEP consisted of larger (diameter about 200 μm) yet less numerous pits. It appears that the nucleation rate was minor for the smoothest surface (SSEP). In the case of SSO, the microstructure (Fig. 1(b)) might have contributed to the limited pitting growth observed in this case. Indeed, individual pits of different sizes seemed to have grown through grain boundaries without necessarily leading to pitting coalescence. Conversely, the pitting growth rate seemed higher for SSEP in comparison to the other surfaces. The pitting morphology of the SSM surface presented intermediate features between the other two, yet closer to the SSEP behavior.

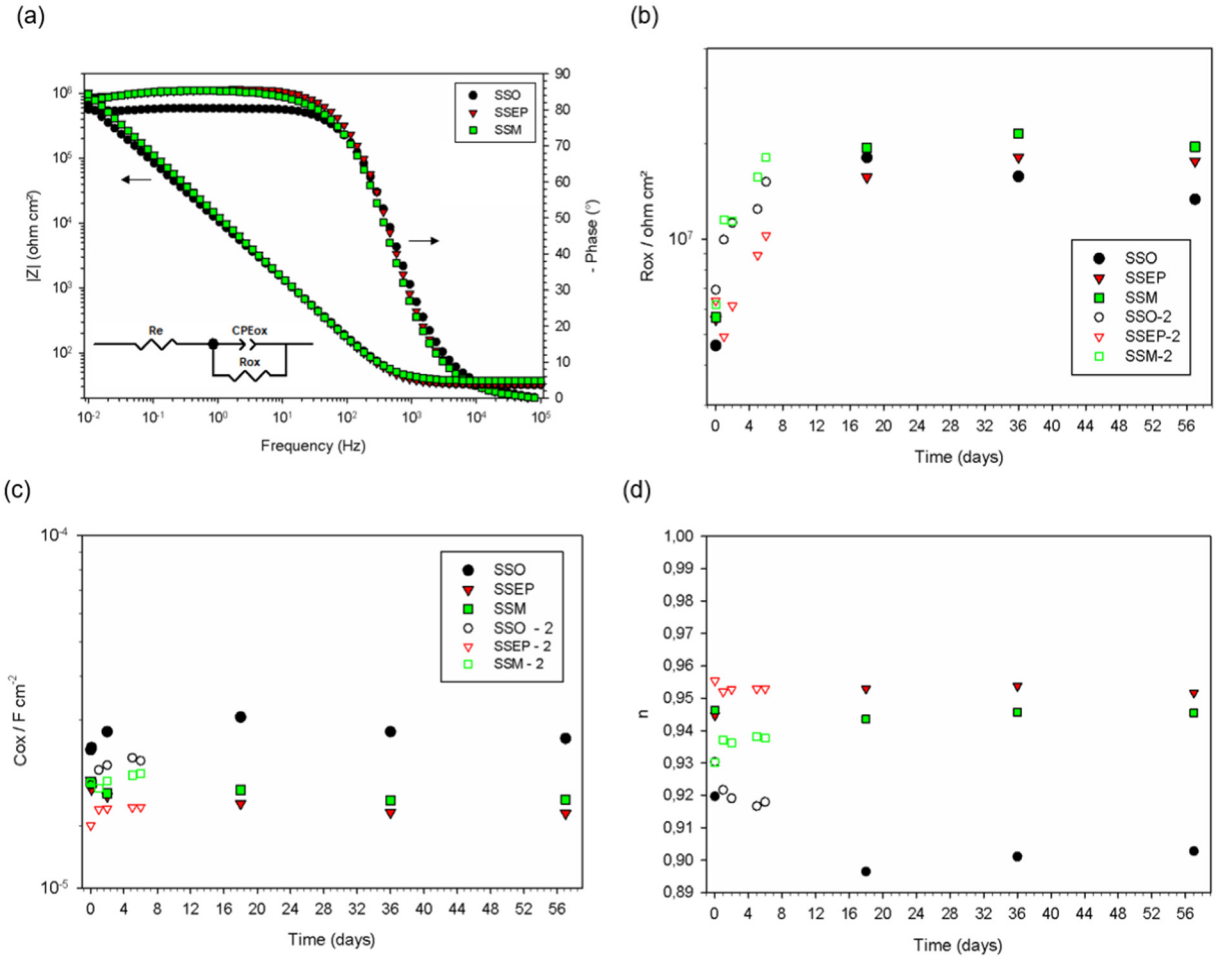

Fig. 8. (a) EIS Bode plot obtained for the 316LSS samples after 30 min of exposure to 0.5 M NaCl. The impedance magnitude and the phase angle are displayed on left and right sides of the diagram, respectively. The presented Equivalent Electrical Circuit was used to fit the impedance data. R_e: electrolyte resistance; R_{ox} and CPE_{ox} are the resistance and the parameter associated with the capacitive properties of the passive oxide film, respectively. (b, c, d) Evolution of EIS fitted parameters obtained from duplicate experiments: R_{ox} (b), C_{ox} (c) and n (d).

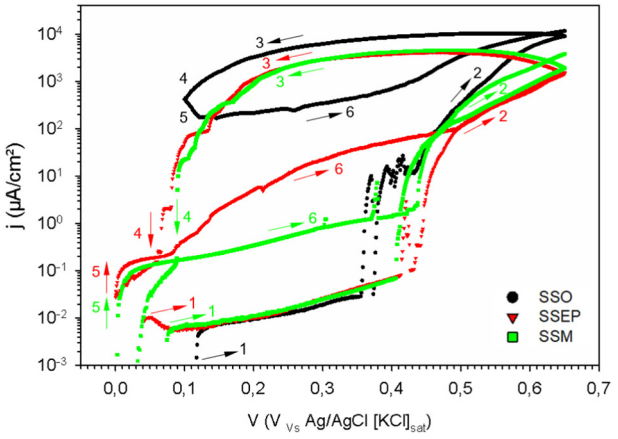

Fig. 9. Anodic cyclic voltammetry curves of the different 316L treated surfaces (SSO, SSEP, SSM) obtained in 0.5 M NaCl solution after 58 days of immersion. The distinct scans are indicated by arrows: 1 and 2 (first forward sweep); 3 and 4 (back sweep); 5 and 6 (second forward sweep).

Most importantly, the pitting process developed on SSO yielded pits of considerable deepness. On the contrary, the pits observed for SSEP and SSM were considerably smoother and seemed to be relatively shallower. These distinct morphological features of pitting correlated well with the distinct passivation behavior highlighted by the CV analysis carried out on the three surfaces (Fig. 9).

3.5.2. Mott-Schottky analysis

Despite the important role that microstructure might have played on the pitting and repassivation behavior of 316LSS specimens, the chemistry of the passive layers should also be considered. Concerning stainless steels, the kinetics of repassivation has been reported to be particularly dependent on presence of alloying elements [53]. Thereby, Mott-Schottky method was applied to correlate the semiconductor properties of the treated surfaces to the composition of the passive layers determined by XPS analysis [23]. Fig. 11 exhibits Mott-Schottky plots measured by sweeping in the positive direction starting from −0.45 V up to +0.40 V (Vs Ag/AgCl/KCl_{sat}) in 0.5 M NaCl. It was decided to avoid excessively high anodic/cathodic overpotentials, as these could lead to eventual modifications of the industrially treated surfaces [24,25].

Based on the point defect model [54,55], the passive oxide film can be considered as a semiconductor material. Hence, according to the electron band theory [22], linear regions on the Mott-Schottky plots represent variations of the width of the space charge layer of the oxide films on the surfaces. When the number of electrons in the conduction band is higher than the number of holes in the valence band, the material can be considered as n-type semiconductor; when the opposite situation is true, it consists of a p-type semiconductor.

From −0.45 V to ~+0.3 V, the passive films of all specimens clearly behaved as n-type semiconductors, which was translated by the

Table 4
Electrochemical parameters obtained by anodic cyclic voltammetry curves of the different 316L treated surfaces (SSO, SSEP, SSM) obtained in 0.5 M NaCl solution after 58 days of immersion.

Parameter	E_{corr}-1 (V)	E_c-1 (V)	ΔE-1 (μA/cm^2)	j_{-650}-1 (μA/cm^2)	E_{corr}-2 (V)	E_c-2 (V)	ΔE-2 (μA/cm^2)	j_{-650}-2 (μA/cm^2)
SSO	0.118	0.359	0.241	9286	0.098	–	–	11,747
SSEP	0.038	0.413	0.375	1388	−0.003	0.082	0.085	1581
SSM	0.075	0.404	0.329	1950	−0.002	0.420	0.422	4048

positive slopes of the curves. At the potential range corresponding to the samples' OCPs, between −0.20 and –0.05 V (Fig. 7), apparent changes in the slopes were observed. This reflected the increasingly higher oxidation reactions that started to trigger the dissolution of particular phases and the renewal of oxides, thus changing the overall electronic character of the surfaces [56]. The origin of the two slopes obtained for passive films formed on stainless steels in the anodic domain appears to be the subject of debate [57]. Turning potentials were depicted at around +0.30 V, highlighting the change in behavior from n-type to p-type for all surfaces [21]. This phenomenon was caused by intense degradation of the passive films and the concomitant formation of oxide phases presenting different compositions/structures. As summarized by Luo et al. [25], such appearance of second donor level might be due to an in-homogeneous donor distribution in passive film and/or to the existence of existing two donor levels in the band gap.

The following Mott-Schottky analysis aimed at identifying the electronic properties of the industrially formed passive films and not those of oxide layers formed upon corrosion. Therefore, in what follows, interpretations considered only the region comprised below the OCP potentials (lower than −0.05 V).

By comparing the curves' slopes, it was possible to infer that SSEP presented the lowest donor density (highest slope) while SSO presented the highest donor density (lowest slope). From specialized literature on the correlation of composition with semiconductor properties of passive films [22,58–60], Fe and Mo-based oxides might equally behave as n-type or p-type semiconductors depending on the type of oxide compound. However, Cr and Ni pure oxides (Cr_2O_3 and NiO) are invariable referred as presenting p-type properties [24].

Therefore, by plotting the atomic fraction of Cr + Ni as determined by XPS analysis (Fig. 11(b)), it was observed that SSEP had the highest fraction of elements forming oxides presenting p-type behavior, while SSO showed the lowest fraction of elements demonstrating this character. It is important to emphasize that this hypothesis holds true only if one considers the first ~4 nm from the top surfaces; which corresponds well with the estimated thicknesses of the passive films (Fig. 2).

As the treated surfaces certainly comprise oxides presenting both n-type and p-type behaviors, one might consider that the determined n-type behaviors in fact derived from greater overall contributions of donors with respect to acceptors. Therefore, as SSEP presented the lowest donor density, consequently, it also presented the lowest proportion in n-type compounds and likely the highest proportion in p-type compounds. Conversely, SSO exhibited the highest donor density and thus the lowest proportion in p-type compounds. Interestingly, these interpretations from the cathodic branch of the Mott-Schottky plots (Fig. 11(a)) were in good agreement with the XPS profiling of the passive layers displayed in Fig. 11(b) (combined proportion of elements contributing for p-type behavior). For instance, the fact that SSM presented an intermediate contribution from p-type compounds is likely the result of its high Cr content combined with its low Ni content.

4. Conclusions

This study showed that the electropolishing and micro-undulation procedures significantly impact the superficial properties of cold-rolled 316L stainless steel. The surface treatments here addressed were responsible for changing topographical features and also the

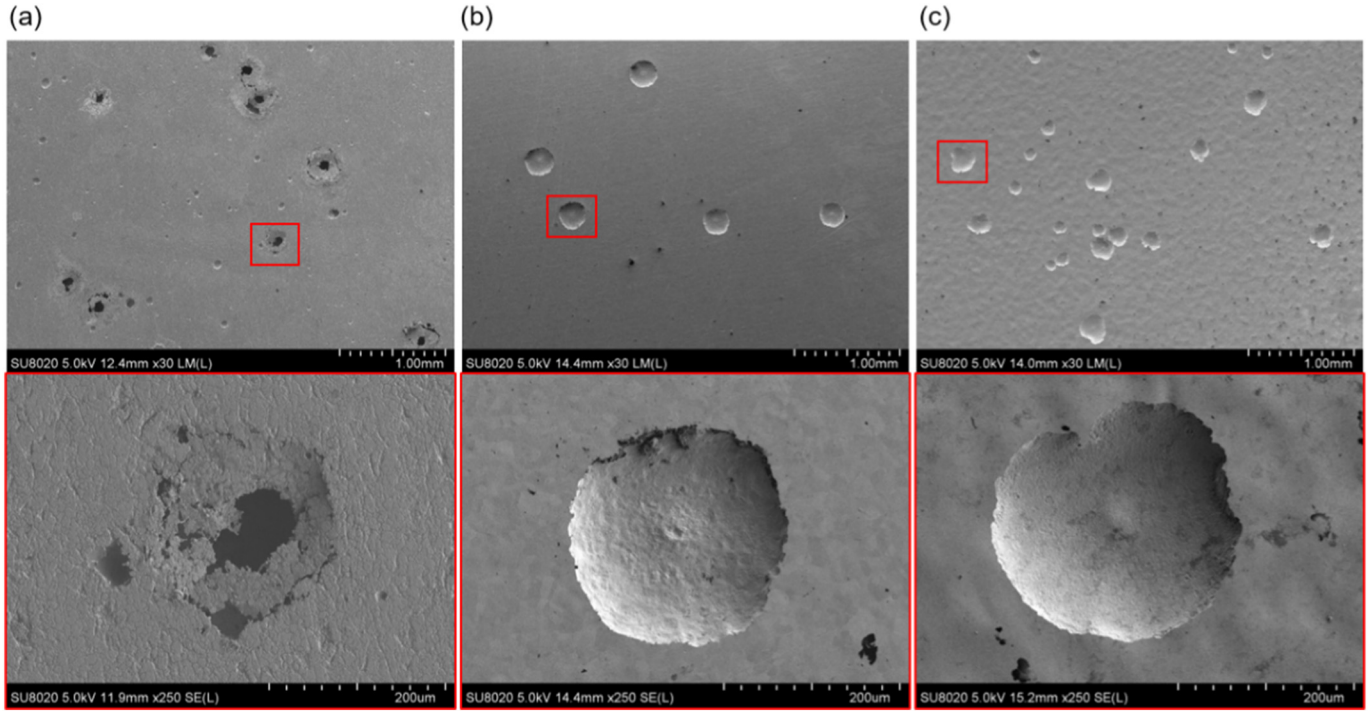

Fig. 10. SEM secondary electron images of the 316L surfaces after 15 min of anodic potentiostatic polarization at +0.8 V in 0.5 M NaCl. (a) SSO; (b) SSEP; (c) SSM.

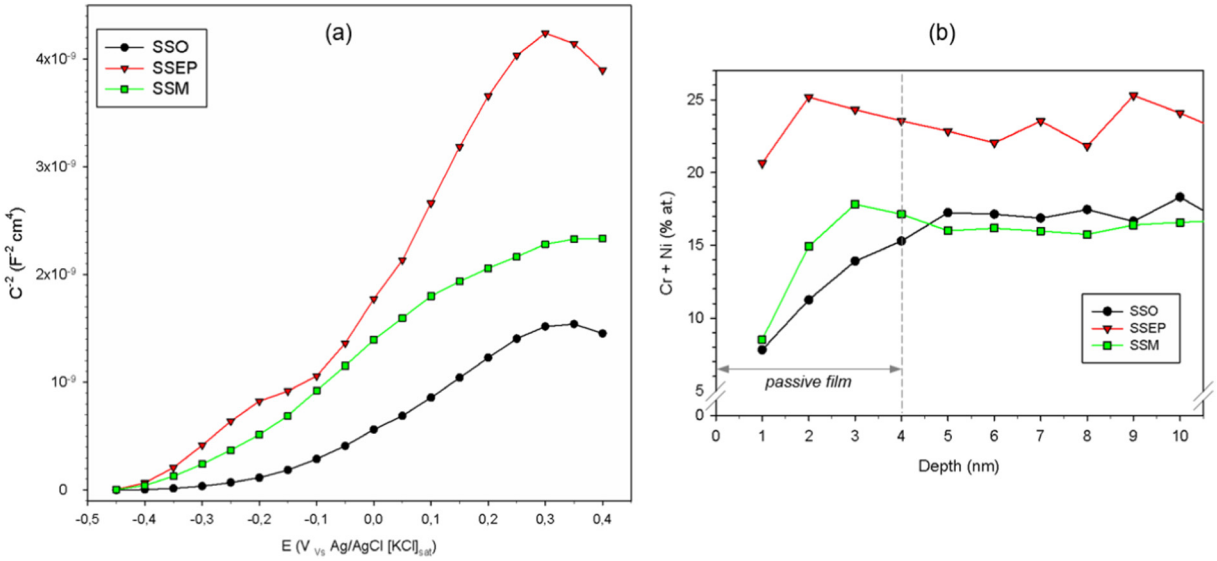

Fig. 11. (a) Mott–Schottky plots for the 316L treated surfaces obtained in the positive direction during 15 min of immersion in 0.5 M NaCl solution. (b) XPS profiling data presenting the elemental ratio of Cr + Ni (at.%) for SSO, SSEP and SSM. Estimation of the thickness of the passive films is included in (b).

microstructure/chemistry of the near-surface zones (at least 10 nm down from the top-surfaces).

The most obvious alteration was the reduced roughness of SSEP samples and the increased roughness/waviness parameters of SSM. Furthermore, as demonstrated by nanoindentation, the micro-undulated surface demonstrated superior hardness in comparison to the others. The enhanced mechanical response of SSM corresponded to the extensive plastic deformation evidenced by the microstructure (twinning). The uniformity of the passive film of SSEP was confirmed by its fracture behavior, as pop-in events were systematically observed (around 6 nm) in the load-displacement curves, indicating through-thin film fracture of the oxide layer. This response was attributed to the combination of the composition and microstructural features observed on the electropolished surface.

Concerning the corrosion behavior tested in 0.5 M NaCl, first, the passive films related to SSEP and SSM showed relatively superior protective properties in comparison to SSO, as illustrated by the evolution of fitted parameters from electrochemical impedance spectroscopy analysis. Moreover, the anodic cyclic voltammetry study highlighted the enhanced repassivation ability of SSEP and particularly of SSM in comparison to the reference surface. These findings were corroborated by the pitting morphology of specimens that were let to corrode under potentiostatic anodic polarization. As indicated by the XPS analysis, the improvement of the anti-corrosion properties of SSEP and SSM was most likely related to the enrichment of their passive films in Cr, and Cr and Mo, respectively. Finally, Mott-Schottky analysis correlated the composition of the passive layers and their semiconductor character. For instance, SSEP simultaneously presented the lowest donor density and the highest proportion of elements (Cr and Ni) contributing for p-type behavior.

The interesting combination of high surface hardness with enhanced corrosion resistance determined for SSM might explain the superior behavior of the micro-undulated surface in tribocorrosion applications, as claimed by industrial users of this surface finish technology. However, future studies should assess the performance of the treated surfaces under tribocorrosion solicitations close to the ones encountered in real applications.

Author contributions section

L.B. Coelho: Conceptualization, Methodology, Validation, Investigation, Writing - Original Draft, Visualization.

S. Kossman: Conceptualization, Methodology, Validation, Formal analysis, Writing - Original DraftInvestigation, Visualization.

A. Mejias: Validation, Writing - Review & Editing.

X. Noirfalise: Investigation, Writing - Review & Editing.

A. Montagne: Validation, Writing - Review & Editing.

A. Van Gorp: Investigation, Writing - Review & Editing.

M. Poorteman: Conceptualization, Resources, Writing - Review & Editing, Project administration, Funding acquisition.

M.-G. Olivier: Validation, Writing - Review & Editing, Supervision.

Declaration of competing interest

The authors declare that they have no known competing financial interests or personal relationships that could have appeared to influence the work reported in this paper.

Acknowledgments

The authors acknowledge the Interreg France-Wallonie-Vlaanderen program, TRANSPORT, with the financial support of the European Regional Development Fund (ERDF). Packo Inox is acknowledged for providing stainless steel treated plates. The author L.B. Coelho acknowledges Mrs. Amandine Portier for preparing specimens for electrochemical testing. Authors would like to thank Prof. Alain Iost for fruitful discussions in the subject of indentation and microstructural analysis.

References

[1] Global Stainless Steel Production, Statista, n.d https://www.statista.com/statistics/223028/world-stainless-steel-production, (2018) , Accessed date: 5 August 2019.
[2] V.B. Welding, Manual for surface treatment of stainless steels, n.d.
[3] A. Kosmač, Electropolishing Stainless Steels, Brussels Euro Inox, 2010.
[4] S.S.D.K. Popov, B. Grgur, Fundamental Aspects of Electrometallurgy, Springer, US, 2002.
[5] A. Heydari Astaraee, R. Miresmaeili, S. Bagherifard, M. Guagliano, M. Aliofkhazraei, Incorporating the principles of shot peening for a better understanding of surface mechanical attrition treatment (SMAT) by simulations and experiments, Mater. Des. 116 (2017) 365–373, https://doi.org/10.1016/j.matdes.2016.12.045.
[6] T. Balusamy, T.S.N. Sankara Narayanan, K. Ravichandran, I.S. Park, M.H. Lee, Influence of surface mechanical attrition treatment (SMAT) on the corrosion behaviour of AISI 304 stainless steel, Corros. Sci. 74 (2013) 332–344, https://doi.org/10.1016/j.corsci.2013.04.056.
[7] R.S. Yassar, L. Scudiero, A.S. Alamr, D.F. Bahr, M.G. Norton, Microstructure–mechanical and chemical behavior relationships in passive thin

films, Thin Solid Films 518 (2010) 2757–2763, https://doi.org/10.1016/j.tsf.2009.08.032.
[8] E.-S. Lee, Machining characteristics of the electropolishing of stainless steel (STS316L), Int. J. Adv. Manuf. Technol. 16 (2000) 591–599, https://doi.org/10.1007/s001700070049.
[9] S.-J. Lee, J.-J. Lai, The effects of electropolishing (EP) process parameters on corrosion resistance of 316L stainless steel, J. Mater. Process. Technol. 140 (2003) 206–210, https://doi.org/10.1016/S0924-0136(03)00785-4.
[10] L.R. Hilbert, D. Bagge-Ravn, J. Kold, L. Gram, Influence of surface roughness of stainless steel on microbial adhesion and corrosion resistance, Int. Biodeterior. Biodegradation 52 (2003) 175–185, https://doi.org/10.1016/S0964-8305(03)00104-5.
[11] M.B. Leban, Č. Mikyška, T. Kosec, B. Markoli, J. Kovač, The effect of surface roughness on the corrosion properties of type AISI 304 stainless steel in diluted NaCl and urban rain solution, J. Mater. Eng. Perform. 23 (2014) 1695–1702, https://doi.org/10.1007/s11665-014-0940-9.
[12] Y. Sun, R. Bailey, Improvement in tribocorrosion behavior of 304 stainless steel by surface mechanical attrition treatment, Surf. Coatings Technol. 253 (2014) 284–291, https://doi.org/10.1016/j.surfcoat.2014.05.057.
[13] A.Y. Chen, W.F. Hu, D. Wang, Y.K. Zhu, P. Wang, J.H. Yang, X.Y. Wang, J.F. Gu, J. Lu, Improving the intergranular corrosion resistance of austenitic stainless steel by high density twinned structure, Scr. Mater. 130 (2017) 264–268, https://doi.org/10.1016/j.scriptamat.2016.11.032.
[14] S. Bagherifard, S. Slawik, I. Fernández-Pariente, C. Pauly, F. Mücklich, M. Guagliano, Nanoscale surface modification of AISI 316L stainless steel by severe shot peening, Mater. Des. 102 (2016) 68–77, https://doi.org/10.1016/j.matdes.2016.03.162.
[15] H. Search, C. Journals, A. Contact, M. Iopscience, I.P. Address, Electrochemical and materials aspects of tribocorrosion systems, 3121 (2006), https://doi.org/10.1088/0022-3727/39/15/S01.
[16] D. Landolt, S. Mischler, M. Stemp, Electrochemical methods in tribocorrosion: a critical appraisal, Electrochim. Acta 46 (2001) 3913–3929, https://doi.org/10.1016/S0013-4686(01)00679-X.
[17] B. Bhushan, Introduction to Tribology, second, John Wiley & Sons Inc, Chichester, West Sussex, United Kingdom, 2013.
[18] M. Packo, I. Quaghebeur, Micro-undulation, https://www.electropolish.be/en/surface-treatments/per-surface-treatment/micro-ondulation, (2016).
[19] ASTM A480/A480M-08b, Standard Specification for General Requirements for Flat-Rolled Stainless and Heat-Resisting Steel Plate, Sheet, and Strip, West Conshohocken, PA, (2008), https://doi.org/10.1520/A0480_A0480M-08B.
[20] 2B, 2D and BA Cold Rolled Finishes, (n.d.). https://www.assda.asn.au/technical-info/surface-finishes/2b-2d-and-ba-cold-rolled-finishes (accessed July 29, 2019).
[21] H.X. Guo, B.T. Lu, J.L. Luo, Study on passivation and erosion-enhanced corrosion resistance by Mott-Schottky analysis, Electrochim. Acta 52 (2006) 1108–1116, https://doi.org/10.1016/j.electacta.2006.07.026.
[22] Z. Feng, X. Cheng, C. Dong, L. Xu, X. Li, Passivity of 316L stainless steel in borate buffer solution studied by Mott-Schottky analysis, atomic absorption spectrometry and X-ray photoelectron spectroscopy, Corros. Sci. 52 (2010) 3646–3653, https://doi.org/10.1016/j.corsci.2010.07.013.
[23] J.S. de Souza, L.A. de Oliveira, I.J. Sayeg, R.A. Antunes, Electrochemical study of the AISI 409 ferritic stainless steel: passive film stability and pitting nucleation and growth, Mater. Res. 20 (2017) 1669–1680, https://doi.org/10.1590/1980-5373-mr-2017-0204.
[24] L.V. Taveira, M.F. Montemor, M. Da Cunha Belo, M.G. Ferreira, L.F.P. Dick, Influence of incorporated Mo and Nb on the Mott-Schottky behaviour of anodic films formed on AISI 304L, Corros. Sci. 52 (2010) 2813–2818, https://doi.org/10.1016/j.corsci.2010.04.021.
[25] H. Luo, X. Wang, C. Dong, K. Xiao, X. Li, Effect of cold deformation on the corrosion behaviour of UNS S31803 duplex stainless steel in simulated concrete pore solution, Corros. Sci. 124 (2017) 178–192, https://doi.org/10.1016/j.corsci.2017.05.021.
[26] S.P. Harrington, T.M. Devine, Analysis of electrodes displaying frequency dispersion in Mott-Schottky tests, J. Electrochem. Soc. 155 (2008) C381, https://doi.org/10.1149/1.2929819.
[27] S. Gao, C. Dong, H. Luo, K. Xiao, X. Li, Electrochemical behavior and nonlinear Mott-Schottky characterization of a stainless steel passive film, Anal. Lett. 47 (2014) 1162–1181, https://doi.org/10.1080/00032719.2013.865201.
[28] Z. Qingdong, M. Rohwerder, Z. Zhao, Z. Jin, Semiconducting behavior of temporarily protective oil coating on the surface of AISI 304 stainless steel in 5% Na [sub 2]SO[sub 4] solution during its degradation, J. Electrochem. Soc. 151 (2004) B446, https://doi.org/10.1149/1.1756889.
[29] Bio-Logic Science Instruments, Application of the Capacitance-Voltage Curve to Photovoltaic Cell Characterizations, 5 (2018) https://www.bio-logic.net/wp-content/uploads/20110609-Application-note-35.pdf.
[30] A01 Committee: ASTM A480/A480M-18a, Standard Specification for General Requirements for Flat-Rolled Stainless and Heat-Resisting Steel Plate, Sheet, and Strip, West Conshohocken, PA, (2018).
[31] D. C, M. Helzel, Guide to Stainless Steel Finishes, (2005).
[32] D. Gallitelli, D. Retraint, E. Rouhaud, Comparison between conventional shot peening (SP) and surface mechanical attrition treatment (SMAT) on a titanium alloy, Adv. Mater. Res. 996 (2014) 964–968. doi:10.4028/www.scientific.net/AMR.996.964.
[33] S. Mischler, A. Spiegel, D. Landolt, The role of passive oxide films on the degradation of steel in tribocorrosion systems, Wear. 225–229 (1999) 1078–1087, https://doi.org/10.1016/S0043-1648(99)00056-3.
[34] A. Alamr, D.F. Bahr, M. Jacroux, Effects of alloy and solution chemistry on the fracture of passive films on austenitic stainless steel, Corros. Sci. 48 (2006) 925–936, https://doi.org/10.1016/j.corsci.2005.02.018.
[35] B. Chatterjee, Science and Industry of Electropolishing, n.d.
[36] S. Habibzadeh, L. Li, D. Shum-Tim, E.C. Davis, S. Omanovic, Electrochemical polishing as a 316L stainless steel surface treatment method: towards the improvement of biocompatibility, Corros. Sci. 87 (2014) 89–100, https://doi.org/10.1016/j.corsci.2014.06.010.
[37] W. Han, F. Fang, Fundamental aspects and recent developments in electropolishing, Int. J. Mach. Tools Manuf. 139 (2019) 1–23, https://doi.org/10.1016/j.ijmachtools.2019.01.001.
[38] R.T. Loto, Pitting corrosion resistance and inhibition of lean austenitic stainless steel alloys, Austenitic Stainl. Steels - New Asp, 2017.
[39] A. Pardo, M.C. Merino, A.E. Coy, F. Viejo, R. Arrabal, E. Matykina, Effect of Mo and Mn additions on the corrosion behaviour of AISI 304 and 316 stainless steels in H2SO4, Corros. Sci. 50 (2008) 780–794, https://doi.org/10.1016/j.corsci.2007.11.004.
[40] M.I. Hazza, M.E. El-Dahshan, The effect of molybdenum on the corrosion behaviour of some steel alloys, Desalination 95 (1994) 199–209, https://doi.org/10.1016/0011-9164(94)00014-X.
[41] W. Zuocheng, F. Di-Franco, A. Seyeux, S. Zanna, V. Maurice, P. Marcus, Passivation-induced physicochemical alterations of the native surface oxide film on 316L austenitic stainless steel, Eurocorr 2019, 2019.
[42] C.P. Dillon, Corrosion Resistance of Stainless Steels, CRC Press, 1995.
[43] E. Aghababaie, H.R. Javadinejad, M. Saboktakin Rizi, M. Ebrahimian, Effect of chlorine ion on the corrosion of 316L austenitic stainless steel, Adv. Eng. Forum. 23 (2017) 1–12, https://doi.org/10.4028/www.scientific.net/AEF.23.1.
[44] Profile roughness parameters - Surface Metrology Guide - Digital Surf, (n.d.).
[45] A.C. Fischer-Cripps, Nanoindentation, 3rd ed., Springer, New York, 2011, pp. 21–37.
[46] W.C. Oliver, G.M. Pharr, Measurement of hardness and elastic modulus by instrumented indentation: advances in understanding and refinements to methodology, J. Mater. Res. 19 (2004) 3–20, https://doi.org/10.1557/jmr.2004.19.1.3.
[47] Y. Wu, B. Guelorget, Z. Sun, R. Déturche, D. Retraint, Characterization of gradient properties generated by SMAT for a biomedical grade 316L stainless steel, Mater. Charact. 155 (2019) 109788, , https://doi.org/10.1016/j.matchar.2019.109788.
[48] J.L. Loubet, M. Bauer, A. Tonck, S. Bec, B. Gauthier-Manuel, Nanoindentation with a surface force apparatus, Mech. Prop. Deform. Behav. Mater. Having Ultra-Fine Microstruct, Springer, Netherlands, Dordrecht, 1993, pp. 429–447, , https://doi.org/10.1007/978-94-011-1765-4_28.
[49] S. Bec, A. Tonck, J.-M. Georges, E. Georges, J.-L. Loubet, Improvements in the indentation method with a surface force apparatus, Philos. Mag. A. 74 (1996) 1061–1072, https://doi.org/10.1080/01418619608239707.
[50] D.F. Bahr, D.E. Kramer, W.W. Gerberich, Non-linear deformation mechanisms during nanoindentation, Acta Mater. 46 (1998) 3605–3617, https://doi.org/10.1016/S1359-6454(98)00024-X.
[51] Y. Yao, X. Cao, L. Qiao, W. Chu, Yield point phenomena during nanoidentation, Tribol. Trans. 47 (2004) 239–247, https://doi.org/10.1080/05698190490439148.
[52] M.L. Zheludkevich, K.A. Yasakau, Triazole and thiazole derivatives as corrosion inhibitors for AA2024 aluminium alloy, 47 (2005) 3368–3383, https://doi.org/10.1016/j.corsci.2005.05.040.
[53] H. Xu, D. Sun, H. Yu, Repassivation behavior of 316L stainless steel in borate buffer solution: kinetics analysis of anodic dissolution and film formation, Appl. Surf. Sci. 357 (2015) 204–213, https://doi.org/10.1016/j.apsusc.2015.09.018.
[54] Y. Gui, Z.J. Zheng, Y. Gao, The bi-layer structure and the higher compactness of a passive film on nanocrystalline 304 stainless steel, Thin Solid Films 599 (2016) 64–71, https://doi.org/10.1016/j.tsf.2015.12.039.
[55] I. Nicic, D.D. Macdonald, The passivity of type 316L stainless steel in borate buffer solution, J. Nucl. Mater. 379 (2008) 54–58, https://doi.org/10.1016/j.jnucmat.2008.06.014.
[56] L. Hongyun, Z. Yubo, L. Hongdou, L. Jinlong, M. Yue, Characterization of the oxide films formed on low temperature sensitized AISI 321 stainless steel with different strain levels in elevated temperature borate buffer solution, J. Alloys Compd. 696 (2017) 1235–1243, https://doi.org/10.1016/j.jallcom.2016.12.107.
[57] A. Fattah-Alhosseini, S. Vafaeian, Comparison of electrochemical behavior between coarse-grained and fine-grained AISI 430 ferritic stainless steel by Mott-Schottky analysis and EIS measurements, J. Alloys Compd. 639 (2015) 301–307, https://doi.org/10.1016/j.jallcom.2015.03.142.
[58] P. Schmuki, Electrochemical behavior of Cr[sub 2]O[sub 3]/Fe[sub 2]O[sub 3] artificial passive films studied by in situ XANES, J. Electrochem. Soc. 145 (1998) 791, https://doi.org/10.1149/1.1838347.
[59] K. Sugimoto, Corrosion resistance of artificial passivation films of Fe[sub 2]O[sub 3]-Cr[sub 2]O[sub 3]-NiO formed by metalorganic chemical vapor deposition, J. Electrochem. Soc. 140 (1993) 1586, https://doi.org/10.1149/1.2221606.
[60] F. Di Quarto, S. Piazza, C. Sunseri, A photocurrent spectroscopic investigation of passive films on chromium, Corros. Sci. 31 (1990) 721–726, https://doi.org/10.1016/0010-938X(90)90187-A.